Dealing With δ-Scuti Variables: Transit Light Curve Analysis of Planets Orbiting Rapidly Rotating, Seismically Active A/F Stars

John P. Ahlers[1,2], Jason W. Barnes[1] , and Samuel A. Myers[1]

[1] Physics Department, University of Idaho, Moscow, ID 83844, USA

[2] Exoplanets and Stellar Astrophysics Laboratory, Code 667, NASA Goddard Space Flight Center, Greenbelt, MD 20771, USA

Abstract

We measure the bulk system parameters of the seismically active, rapidly rotating δ-Scuti KOI-976 and constrain the orbit geometry of its transiting binary companion using a combined approach of asteroseismology and gravity-darkening light curve analysis. KOI-976 is a $1.62 \pm 0.2\,M_\odot$ star with a measured $v\sin(i)$ of $120 \pm 2\,\mathrm{km\,s}^{-1}$ and seismically induced variable signal that varies by $\sim0.6\%$ of the star's total photometric brightness. We take advantage of the star's oblate shape and seismic activity to perform three measurements of its obliquity angle relative to the plane of the sky. We first apply a rotational splitting theory to the star's variable signal observed in short-cadence *Kepler* photometry to constrain KOI-976's obliquity angle, and then subtract off variability from that data set using the linear algorithm for significance reduction software LASR. We perform gravity-darkened fits to *Kepler* variability-subtracted short-cadence photometry and to *Kepler's* phase-folded long-cadence photometry to obtain two more measurements of the star's obliquity. We find that the binary system transits in a grazing configuration with measured obliquity values of $36° \pm 17°$, $46° \pm 16°$, and $43° \pm 20°$, respectively, for the three measurements. We perform these analyses as a way to demonstrate overcoming the challenges high-mass stars can present to transit light curve fitting and to prepare for the large number of exoplanets that the *Transiting Exoplanet Survey Satellite* will discover orbiting A/F stars.

Key words: planets and satellites: detection – planets and satellites: fundamental parameters – stars: variables: delta Scuti

1. Introduction

High-mass stars of $\sim1.3\,M_\odot$ present unique challenges to transit light curve analysis that stem from their fundamental structure. In general, stars less massive than the Sun have larger convective zones and smaller radiative zones, and stars more massive than the Sun have larger radiative zones and smaller convective zones (Toomre et al. 1976). However, at masses higher than $\sim1.3\,M_\odot$ the star's carbon–nitrogen–oxygen cycle of nuclear fusion produces an extremely high core temperature, causing the core itself to become convective. This convective core resides inside a radiative region that extends to the star's surface. The result is that these stars are effectively inside-out from their low-mass counterparts, with convective interiors and radiative exteriors. Albrecht et al. (2012) identifies this inversion at a stellar surface temperature of $\sim6200\,\mathrm{K}$. Throughout this work, we use $M_\star \approx 1.3\,M_\odot$ and $T_{\mathrm{eff}} \approx 6200$ as approximate cutoffs for designating a star as high-mass or low-mass.

As a consequence of their structure, high-mass stars have weak external magnetic fields. Solar dynamo theory states that stellar magnetic fields are caused by the convection zone of the star (Charbonneau 2014), so the magnetic field in high-mass stars should be mostly internal near the star's convective core. Recent observations using NASA's *Kepler* telescope corroborate this theory (e.g., Bagnulo et al. 2006; Boehm et al. 2015).

Without a strong external magnetic field, no stellar magnetic braking takes place, allowing high-mass stars to maintain their primordial rotation rates throughout their lifetimes (Mestel 1968). All stars start off spinning quickly during their formation as protostellar material collapses inward (Hansen & Kawaler 1994); however, the external magnetic fields of low-mass stars cause them to slowly decrease their rate of rotation over time (Meibom et al. 2009). This effect, called magnetic braking, occurs when the star's magnetic field transfers angular momentum into an escaping stellar wind. These outflows are stirred by the star's magnetic field, which transfers angular momentum from the star to the outflow, slowing the star's rotation rate. However, angular momentum transfer does not occur between a high-mass star and its outflow, allowing them to stay spinning rapidly throughout their main sequence.

The rotation rates of high-mass stars often hover near their rotational break up speed, with equatorial rotational velocities reaching hundreds of kilometers per second (e.g., Royer et al. 2002; Jackson et al. 2004; Huang & Gies 2006). Their high rotation rates distort their shapes into oblate spheroids that bulge outward at the equator. For example, the well-known rapid rotator Altair spins at 72% of its breakup speed and has an oblateness factor of 0.177, meaning Altair's polar radius is only 82.3% as large as its equatorial radius (Monnier et al. 2007).

The smaller effective surface gravity near a rapid rotator's equator results in a lower stellar effective temperature. The von Zeipel theorem (Von Zeipel 1924) or gravity-darkening law relates surface gravity with effective temperature:

$$T_{\mathrm{eff}} = T_{\mathrm{pole}} \left(\frac{g_{\mathrm{eff}}}{g_{\mathrm{pole}}} \right)^{\beta}, \qquad (1)$$

where β is the so-called gravity-darkening exponent. The star's rapid rotation displaces its hydrostatic equilibrium and induces a pole-to-equator temperature gradient across the stellar surface, resulting in poles that can be several thousand Kelvin hotter than the star's equator. As an example, Altair's stellar

effective temperature varies from ~8500 to 6500 K between its hot poles and cool equator (Kervella et al. 2005).

Additionally, A/F stars can display photometric variability that can obfuscate transit light curve analysis. These stars pulsate with changing light amplitudes that can range from 0.003 to 0.8 mag (Breger 2000), enough to drastically alter or even hide transit events. The most commonly observed variables in the A/F spectral classes are δ-Scuti and their cousins γ-Doradus and dwarf Cepheid variables. NASA's *Kepler* telescope observed over 1400 δ-Scuti stars out of the ~150,000 stars in *Kepler's* field of view (Balona & Nemec 2012).

Previous works have shown that stellar variability seen in δ-Scuti can reveal useful information about a system. Goupil et al. (2000) show that δ-Scuti variables typically oscillate with only a few dominant frequencies, and that the separation between modes can reveal the star's rotation rate and its obliquity relative to the plane of the sky. Zwintz et al. (2014) applied second-order perturbation theory to the intermediate Delta Scuti star HD 144277. Herrero et al. (2011) and others (e.g., Smith et al. 2011; de Mooij et al. 2013; von Essen et al. 2014) have previously combined asteroseismology and exoplanet analysis to characterize WASP-33, a δ-Scuti hosting a transiting hot Jupiter.

Multiple techniques exist for resolving a variable stellar signal in photometry. Previous works on δ-Scuti modeled photometric variability using the iterative fitting process of fitting more and more sinusoids to the time series using linear regression, known as prewhitening (e.g., Machado et al. 2008; Breger 2011, 2016). In this work we apply a similar fitting routine, the linear algorithm for significance reduction (Ahlers et al. 2018), which subtracts stellar oscillations one at a time from photometry using each oscillation's statistical significance in frequency space as a goodness-of-fit parameter.

The *Transiting Exoplanet Survey Satellite* (*TESS*) expects to discover ~2000 exoplanets orbiting A/F stars (Barclay et al. 2018). Most of these exoplanets will likely orbit rapid rotators, and proper modeling of their transit light curves will need to include the gravity-darkening phenomenon (Barnes 2009; Ahlers 2016). As many as ~200 may also transit δ-Scuti and their cousins (Balona & Nemec 2012). Therefore, proper handling of rapid stellar rotation and stellar seismic activity will enable the analysis of a large fraction of exoplanets discovered by *TESS*.

This work demonstrates how to handle both rapid stellar rotation and stellar variability when extracting information from a transit light curve. We show that these phenomena are not merely complications to a model or noise to be subtracted from a signal, but that they can provide useful insight to the bulk properties of a system through the example system *Kepler* Object of Interest (KOI) 976. In Section 2 we detail our asteroseismic approach and demonstrate the advantages of working with short-cadence photometry. In Section 3 we show the results of our work. In Section 4 we discuss expected results when performing these analyses on photometry from NASA's *TESS* mission.

2. Methods

2.1. Observations

In this work, we choose the δ-Scuti KOI-976—KIC 3441784 —as our target system for analysis. The Exoplanet Follow-up

Table 1
Previously Reported Values of KOI-976

Parameter	Value
$M_\star$ ($M_\odot$)	1.62 ± 0.2
$T_{\rm eff}$ (K)	7240 ± 200
Kepler mag	9.729
$v \sin(i)$ (km s^{-1})	120 ± 2
Transit Period (days)	$52.56902 \pm 5 \times 10^{-5}$
Transit Depth (mmag)	29.61 ± 0.19

Note. $M_\star$, $T_{\rm eff}$, and $v \sin(i)$ were measured with the trans-atlantic exoplanet survey (TReS) telescope and are listed on the ExoFOP.

Observing Program (ExoFOP) lists this system as an eclipsing binary consisting of an F0 star and an M-dwarf companion. The F0 star (hereafter called the primary star) is rotating rapidly with an ExoFOP-reported $v \sin(i)$ of 120 km s^{-1} and seismically induced amplitude variations of ~3.0 mmag. Additionally, ExoFOP identifies the primary star as a high-amplitude δ-Scuti variable (HAD); however, HADs typically have low $v \sin(i)$ and amplitude variations larger than 0.3 mag (Pigulski et al. 2006). Thus we classify KOI-976 as a δ-Scuti but not a HAD. Baranec et al. (2016) identify a binary companion (hereafter called the transiting star) that transits the primary star once every 52.6 days. We list all previously reported values of KOI-976 in Table 1.

KOI-976 serves as an ideal candidate for this analysis for several reasons. The primary star is a poster child for δ-Scuti with a dominant oscillation period of ~1.1 hr and total changes in the star's photometric brightness of ~0.6%. Like most δ-Scuti, KOI-976's seismic activity is dominated by only a few low-degree oscillations. ExoFOP lists the primary star's *Kepler* magnitude as 9.7, providing an excellent signal-to-noise in both *Kepler's* long-cadence and short-cadence data sets. Additionally, the transiting companion provides a transit depth of 30 mmag, making the transit event easy to resolve out of the primary star's variable signal.

In this analysis, we make use of both *Kepler's* long-cadence and short-cadence photometric data sets of KOI-976. The thirty-minute long-cadence photometry of KOI-976 spans NASA's primary *Kepler* mission with Q0-Q17 observations of 27 transit events from 2009 May to 2013 April. We include the entire Q0-Q17 long-cadence data set in our analysis. *Kepler's* one-minute short-cadence photometry of KOI-976 includes Q8 and Q9 observations in early 2011. However, these data sets have a large observation gap between the two quarters, and since only the Q9 short-cadence data set contains a transit, we do not include the Q8 data set in this work.

2.2. Binary Time Delay

Balona (2014) identified a previously unknown binary companion in the KOI-976 system with a 208-day orbit period. They found that this third star in the system contains sufficient angular momentum to significantly shift the location of the system barycenter. They discovered this third star using the time delay method of binary star detection, in which the δ-Scuti's variable photometric signal undergoes phase shifts caused by a speed-of-light delay as is orbits about the barycenter.

Balona (2014) measured that the primary star orbits about the barycenter in an eccentric orbit once every 208 days with a

semimajor axis of 0.27 au, corresponding to a speed-of-light delay that changes by ~200 s throughout the orbit. We account for this effect by adjusting both the long-cadence and short-cadence *Kepler* data sets according to their time delay results. We add/subtract time to each time bin in the data sets according to the primary star's location relative to the system barycenter. See Balona (2014) for the details of our time delay adjustment.

2.3. Asteroseismology

Our asteroseismic analysis of KOI-976 has two main goals: to constrain the primary star's rotation rate and obliquity angle by applying rotational splitting to its out-of-transit variable signal, and to prepare the photometric data set for transit light curve analysis by subtracting off stellar variability. The highest frequency oscillation that can be resolved in *Kepler*'s thirty-minute long-cadence data is defined by its Nyquist rate of 277.8 μHz (Murphy et al. 2013). However, we find in short-cadence that KOI-976 possesses significant frequencies up to ~800 μHz, so in our asteroseismic analysis we exclusively use *Kepler*'s one-minute Q9 short-cadence photometry, which has a cutoff Nyquist rate of 8333.3 μHz.

2.3.1. Rotational Splitting

δ-Scuti typically oscillate at a few dominant frequencies. These frequencies derive from variations in stellar shape that obey the physics of spherical harmonics

$$Y_l^m(\theta, \phi) = \sqrt{\frac{(2l+1)(l-m)!}{4\pi(l+m)!}} P_l^m(\cos(\theta))e^{im\phi}, \qquad (2)$$

where Y describes the oscillation across the star's surface, defined by the azimuthal and polar angles (ϕ, θ), degree l, its order m, and corresponding Legendre polynomial $P_l^m(\cos(\theta))$. For a given degree l, there are $2l+1$ oscillation modes, one for each $-l \leqslant m \leqslant l$ order. Together these grouped oscillations are known as a multiplet. Typically, δ-Scuti are dominated by a few low-degree ($l \lesssim 3$) multiplets. Aerts et al. (2010) offer a detailed explanation of spherical harmonics and multiplets. Burke et al. (2011) previously demonstrated the validity of perturbative methods to model acoustic mode oscillations in rotating δ-Scuti stars, and Ballot et al. (2010) for gravity modes.

For a nonrotating star, all $2l+1$ modes in a multiplet oscillate at the same frequency (Aerts et al. 2010). For example, the $l=1$ multiplet contains a standing $m=0$ wave and prograde $m=1$ and retrograde $m=-1$ waves that run longitudinally across the stellar surface. However, stellar rotation is an additive effect with the $m=1$ and $m=-1$ running waves, making the $m=1$ wave appear faster and the $m=-1$ wave appear slower. Therefore, the $m \neq 0$ modes in a multiplet change in frequency, with the negative-order modes decreasing and the positive-order modes increasing. This effect is known as rotational splitting, because in the frequency power spectrum of a photometric data set multiplet modes appear split apart due to stellar rotation. Suárez et al. (2010) showed that rotational splitting in rapidly rotating stars can be used to probe their internal rotation profile.

The amount a multiplet splits apart depends on how fast a star is rotating, with faster rotation resulting in larger $m \neq 0$ frequency shifts. Therefore, multiplets inherently contain

information about a star's rotation rate. For a slow rotator such as our Sun, $m=1$, -1 frequencies shift by tenths of a μHz. However, the rapid rotation that commonly occurs in high-mass stars can result in frequency shifts of several tens of μHz.

Rapid stellar rotation fundamentally changes the physics of stellar oscillations. Multiplets in slow rotators are in equipartition, meaning all $2l+1$ modes oscillate at the same amplitude (e.g., Kamiaka et al. 2019). Therefore, the relative observed amplitude of the $m=0$ mode and the $m \neq 0$ modes depends only on the star's obliquity angle. This property has been used to constrain the orbit geometries of dozens of transiting exoplanets (e.g., Chaplin et al. 2013; Huber et al. 2013; Van Eylen et al. 2014; Campante et al. 2016). However, the assumption of equipartition is not valid in the regime of rapid rotation. Therefore, we unfortunately cannot reliably measure stellar obliquity angles of rapid rotators by comparing the relative amplitudes in a frequency power spectrum.

Fortunately, rotational splitting offers an independent approach for constraining stellar obliquities. Following Goupil et al. (2000) we apply second-order rotational splitting to measure KOI-976's rotation rate,

$$\nu_m = \nu_0 + m(1 - C_{nl})\nu_\star + m^2 D_1 \frac{\nu_\star^2}{\nu_0}, \qquad (3)$$

where ν_i is the $m=i$ angular frequency in a multiplet, $\nu_\star$ is the stellar rotation frequency, and the Ledoux Constant C_{nl} and the second-order splitting constant and D_1 are values that depend on stellar properties (Goupil et al. 2000). δ-Scuti stars often rotate near their breakup speed, so we include a second-order term that accounts for Coriolis and centrifugal force effects that can force rotational splitting to occur asymmetrically between prograde and retrograde modes.

To constrain the rotation frequency of KOI-976, We start with Equation (3) and rearrange into two components by combining $m=(1, -1)$ solutions

$$\frac{\nu_1 - \nu_{-1}}{2} = (1 - C_{nl})\nu_\star \qquad (4)$$

and

$$\frac{\nu_1 + \nu_{-1} - 2\nu_0}{2} = \frac{D_1 \nu_\star^2}{\nu_0}. \qquad (5)$$

Equations (4) and (5) each affect a multiplet in different ways. The first-order term of Equation (4) determines the total magnitude of frequency shifts. The second-order term of Equation (5) affects the symmetry of the shift. For Sun-like stars, Equation (5) is negligible due to the star's low rotation frequency. Goupil et al. (2000) note that rotational velocities $\gtrsim 100$ km s^{-1} require a third-order term in order to accurately model rotational splitting. However, we only apply second-order theory in this work, which increases the uncertainty in our determination of KOI-976's rotational frequency by ~0.14 μHz. Robust modeling of rapid stellar rotation is accessible through the 2D code TOP (e.g., Lignières et al. 2006; Reese et al. 2006), the Adiabatic Code of Oscillation Including Rotation (ACOR; Ouazzani et al. 2012), or the implicit 2D hydrodynamic and hydrostatic code (Deupree 1990; Deupree & Beslin 2010).

We use these equations to constrain the stellar rotation frequency, and then determine the stellar obliquity ψ via

$$\psi = \cos^{-1}\left(\frac{v\sin(i)}{2\pi\nu_\star R_\star}\right). \qquad (6)$$

We obtain the projected rotational velocity $v\sin(i)$ from *Kepler*'s ExoFOP and list the value in Table 1. We detail the results of this analysis in Section 3.2.

2.3.2. Variability Subtraction

KOI-976's *Kepler* photometry displays a significantly variable signal. The δ-Scuti primary star oscillates with a signal that changes photometrically by $\sim$0.6% with a fundamental oscillation period of $\sim$1.1 hr. These oscillations appear clearly in the short-cadence data set; however, the long-cadence data set's low sample rate does not properly resolve variability—in fact, a cursory examination of the long-cadence photometry would lead one to believe that the data set simply has a low signal-to-noise ratio.

Rather than treating the primary star's variable signal as noise, we explicitly subtract KOI-976's modes of oscillation from short-cadence photometry in order to clean the transit light curve for detailed analysis. We consider this method a superior approach over phase-folding and binning the light curve for two reasons. First, phase-folding and binning can be risky when dealing with variability, particularly for oscillation frequencies near integer multiples of either the phase-folding frequency or the data set's original sample frequency. And second, phase-folding and binning to remove stellar variability only works if a data set is sufficiently large to properly average out variability. In the specific case of KOI-976, the long-cadence data set is $\sim$27 times as long as its phase-folding period, which we find to be adequate-length baseline for averaging out stellar variability. However, many exoplanet photometric data sets (such as from NASA's *TESS* or ground-based observations) contain only one or a few transits, so stellar variability cannot be averaged out.

We subtract stellar variability from the short-cadence data set using the variability fitting program LASR (Linear Algorithm for Significance Reduction; Ahlers et al. 2018). This tool, which we developed specifically for subtracting oscillations from δ-Scuti, removes oscillations from photometry one mode at a time by fitting the oscillation frequency, amplitude, and phase (f, a, p) using the mode's statistical significance in frequency space as a goodness-of-fit criterion. By minimizing a given peak in the Lomb–Scargle normalized periodogram of the data, LASR finds the sinusoidal solution that best removes a given mode of oscillation from photometry.

The LASR fitting tool makes one assumption: that the stellar oscillations present in the photometry are well-modeled as a linear combination of sine waves. For δ-Scuti, this assumption is generally considered acceptable (e.g., Breger et al. 2011). The Q9 short-cadence *Kepler* photometric data set spans about 6 weeks; modes of oscillation in δ-Scuti typically do not change noticeably over those timescales. Additionally, δ-Scuti variables typically do not exhibit nonsinusoidal variability such as starspots or flares due to their weak external magnetic fields. Therefore, LASR is well suited to model KOI-976's variable signal.

We apply LASR to *Kepler*'s Q9 photometry of KOI-976 in order to clean the transit of stellar variability. We mask out the transit, working with only the out-of-transit baseline flux. We subtract oscillations modes one at a time from the data set in order of descending amplitude until we reach our statistical significance cutoff of amplitude $\leqslant$0.1σ, where σ is the average one standard deviation uncertainty of our time bins. At that limit, we cannot confidently distinguish between modes of oscillation and noise, so we end our cleaning process there. We then apply our sinusoidal solution to KOI-976's variability to the single transit in Q9 short-cadence photometry and subtract off stellar variability.

Worth noting is that our subtraction of variability from the transit is technically an oversubtraction. During the transit event, the binary companion blocks some of the primary star's flux—and therefore some of the variable signal—effectively decreasing the amplitude of the variable signal seen by *Kepler*. We apply out-of-transit values for the (f, a, p) of oscillation modes, which do not account for the transit event. However, we estimate that this oversubtraction can affect the transit light curve at a *maximum* flux value of 0.18 mmag (versus the transit depth of 30 mmag). We show in our results that our LASR subtraction provides a cleaned transit light curve with a roughly equivalent signal quality as phase-folding and binning the long-cadence data set, and that this approach produces vastly superior results over phase-folding long-cadence data sets with only a handful of available transits.

### 2.4. Transit Light Curve Analysis

We analyze KOI-976's transit light curve with the gravity-darkening technique (Barnes 2009), which accounts for an oblate stellar shape and the pole-to-equator luminosity gradient induced by rapid stellar rotation. It takes advantage of the star's asymmetry in shape and luminosity to constrain the star's obliquity angle and the planet's projected alignment value directly from light curve fitting. Figure 3 of Ahlers et al. (2015) provides definitions of these angles.

We apply the gravity-darkening technique to both the long-cadence and short-cadence *Kepler* time series to test the validity of variability subtraction as a method for preparing transit light curves. Following our previous gravity-darkening work (Barnes et al. 2011, 2015; Ahlers et al. 2014, 2015), we use the light curve fitting package transitfitter, which uses a Levenberg–Marqhardt χ^2 minimization routine to model transit events across rapidly rotating stars.

In our fit of the long-cadence data set, we first adjust the entire time series according to the speed-of-light delay measured by Balona (2014) and described in Section 2.2. We then phase-fold the 27 transits in the time series around KOI-976's ExoFOP-reported orbit period (Table 1). We bin the resulting single transit light curve at 480 s to average out stellar variability and reduce computation time.

For the short-cadence data set, we mask out the single transit in Q9 photometry and subtract off stellar variability based on our results from Section 2.3.2. We propagate our variability solution through the transit and subtract off all measured oscillations.

We find a surprising but interesting anomaly in both the long-cadence and short-cadence transit light curves. Overall the light curves match the standard V-shape of a grazing binary. However, at about 60% of the way through each transit event, a sharp drop in brightness occurs that lasts for roughly 1 hr and then goes away (Figure 1). This artifact appears in the same part of the transit in both variability-subtracted short-cadence
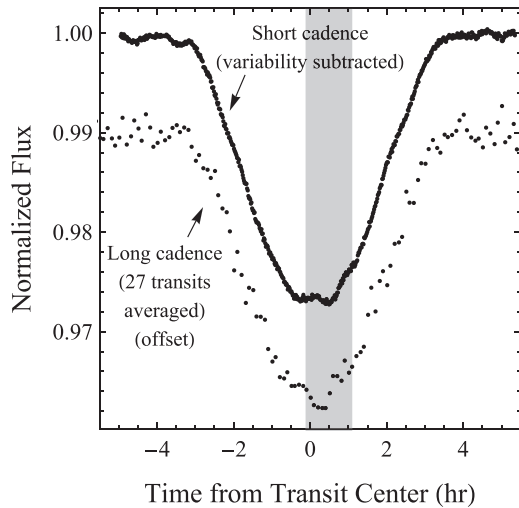
Figure 1. KOI-976 transit light curves displaying the anomaly in their transits. We show the variability-subtracted short-cadence light curve on top and the long-cadence phase-folded transit light curve binned at 480 s below. The gray area marks the unexplained sharp dip in brightness seen in all 27 long-cadence transit events and in the single short-cadence transit event. This repeating signal cannot be explained with our gravity-darkening model or with stellar variability, so we mask out the gray area during our transit analysis. We discuss possible causes of this anomaly in Section 4.2.

data and phase-folded and binned long-cadence data, and so is not easily explained as a systematic in our data sets. The most straightforward explanation is that the dip in brightness is caused by a repeatable astrophysical phenomenon. Stellar gravity-darkening cannot produce this distinct drop in brightness, so we consider its analysis to be outside the scope of this paper. We mask out the unexplained signal when fitting the long-cadence and short-cadence transit light curves, and we discuss possible causes in Section 4.2.

With the short-cadence and long-cadence time series fully prepared for fitting, we apply the gravity-darkening model to the transit light curves. We independently fit long-cadence and short-cadence data to contrast phase-folding and variability subtraction as approaches for handling transit light curves with stellar variability. KOI-976's companion transits in a grazing configuration, therefore we cannot confidently extract information about its eccentricity (Barnes 2007) and assume a circular orbit in our best-fit model. We show the results of our transit light curve analysis in Section 3.3.

3. Results

This work includes a four-stage analysis of KOI-976, a rapidly rotating δ-Scuti with a transiting binary companion observed by *Kepler*. We first measure the primary star's obliquity angle and rotation rate by applying asteroseismic theory to KOI-976's seismically active out-of-transit photometry. We then subtract out stellar variability from KOI-976's short-cadence transit event to prepare the data set for further analysis. Finally, we perform a joint analysis of both the long-cadence and short-cadence *Kepler* transit light curves using a gravity-darkened model to measure bulk parameters of the system and to test the validity of variability subtraction as a path for cleaning transit light curves. We describe our results in the following subsections.

3.1. Asteroseismology

We measure the rotation rate of KOI-976 using second-order rotational splitting and list our results in Table 3. We find the (ν_{-1}, ν_0, ν_1) frequencies of the dominant triplet through inspection of KOI-976's power spectrum, shown in Figure 2 and listed in Table 4. We set an initial range of possible $\nu_{\star}$ values by applying the range of $0.8 \leqslant (1 - C_{nl}) \leqslant 1.0$ for the Ledoux constant, which encompasses both the theoretical and empirical ranges of values expected for δ-Sct stars. This initial range constrains the star's rotation frequency to $18.5\,\mu\text{Hz} \leqslant \nu_{\star} \leqslant 23.1\,\mu\text{Hz}$ through Equation (4).

Only three frequency peaks exist in the possible range of rotation frequencies. Following Breger et al. (2011), we identify the rotation frequency peak to be $21.705\,\mu\text{Hz}$ based on the peak's slightly asymmetric shape and significance (Figure 2 inset). Our identified $\nu_{\star}$ acts as the combination frequency for most of the modes listed in Table 4, further suggesting that the identified peak is the star's rotation frequency. We identify the combination frequencies as a check for identifying KOI-976's rotation frequency and do not consider the combinations listed in Table 4 to be an exhaustive search.

We constrain the primary star's obliquity angle using Equation (6). We use the empirical mass–radius relation (Demircan & Kahraman 1991) to set an approximate range for the stellar radius: $1.48\,R_{\odot} \leqslant R_{\star} \leqslant 1.85\,R_{\odot}$. This range of stellar radii agrees with the short-cadence and long-cadence transit light curve fit results (see Table 2).

3.2. Variability Subtraction

We use the programming tool LASR (Ahlers et al. 2018) to subtract off 204 oscillation modes from KOI-976's Q9 short-cadence *Kepler* photometry. We find the δ-Scuti's variability to be well modeled as a linear combination of sinusoids over the ~six-week data set. We list the best-fit frequencies, amplitudes, and phases of all oscillation modes in Table 4 and show the subtraction results in Figure 3.

3.3. Light Curve Fits

After subtracting stellar variability from KOI-976's short-cadence light curve and masking out the anomalous bump seen in Figure 1, we fit the resulting transit using the gravity-darkening technique. We show the best-fit and residual in Figure 4 and list the results in Table 2.

We also phase-fold KOI-976's long-cadence data set around the ExoFOP-reported orbital period of $52.56902 \pm 5 \times 10^{-5}$ days and bin the light curve at 480 s to average out stellar variability. We fit both data sets with the gravity-darkening model to obtain constraints on stellar radius, companion radius, stellar obliquity, and the companion's projected alignment and inclination angles. For both fits, we use quadratic limb-darkening coefficient values from Sing (2010) and ascribe uncertainties to them based on the star's temperature uncertainty.

We find that KOI-976 is a binary system in a grazing configuration with no secondary eclipse, consistent with previous observations. The *Kepler* telescope provided very high-quality photometry of this system, normally allowing for the detailed analysis of the transit light curve, however, the grazing nature of the transit introduces strong interdependencies in our fitting model between the star's radius and projected
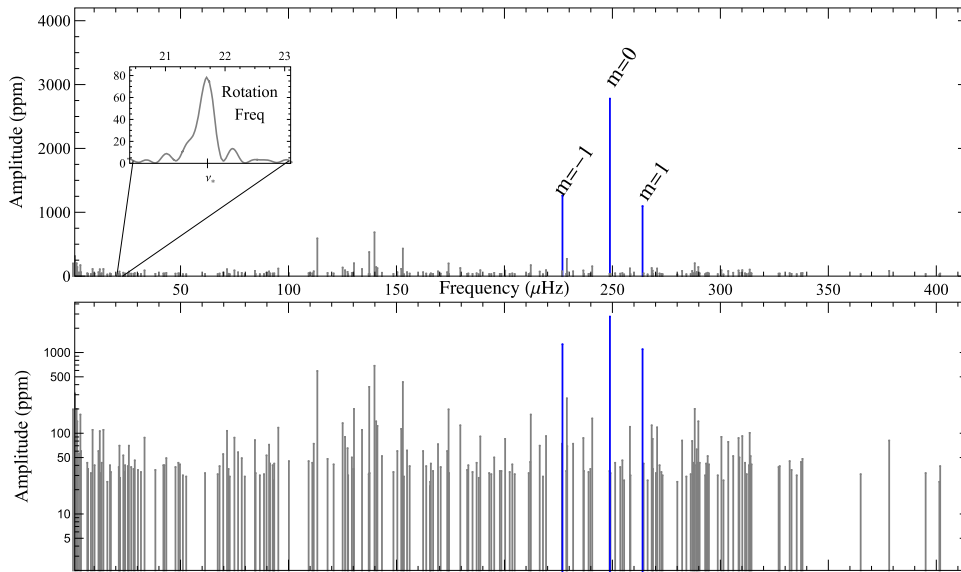
Figure 2. Top: KOI-976's frequency power spectrum. We identify a frequency triplet (shown in blue), with azimuthal modes (*m*) labeled. The triplet displays large-scale and asymmetric rotational splitting, consistent with rapid stellar rotation. We color the triplet's corresponding measured frequencies blue in Table 4. The lower frequency dominant modes in KOI-976's power spectrum do not match the rotational splitting theory (Dziembowski & Goode 1992; Soufi et al. 1998). Bottom: logarithmic plot showing the 204 identified modes of oscillation of KOI-976.

Table 2
Results from the Combined Asteroseismology and Transit Light Curve Analyses

Parameter	Description	Asteroseismology	Short-cadence Fit	Long-cadence Fit
$\chi^2_{\rm red}$	Goodness-of-fit	3.81	3.65	1.94
$R_\star$	Stellar radius ($R_\odot$)	⋯	1.54 ± 0.12	1.59 ± 0.15
R_c	Companion radius ($R_{\rm Jup}$)	⋯	3.3 ± 0.3	3.9 ± 0.4
$\Omega_\star$	Stellar rotation rate (hr)	12.80 ± 0.09	14 ± 3	14 ± 3
$\psi_\star$	Stellar obliquity (deg)	$36° \pm 17°$	$46° \pm 16°$	$43° \pm 20°$
λ	Projected alignment (deg)	⋯	$7° \pm 13°$	$16° \pm 15°$
i	Projected inclination (deg)	⋯	$91°.192 \pm 0°.014$	$91°.28 \pm 0°.03$
c_1	Limb-darkening constant	⋯	$0.56(\pm 0.2)$	$0.56(\pm 0.2)$
c_2	Limb-darkening constant	⋯	$-0.16(\pm 0.2)$	$-0.16(\pm 0.2)$
β	Gravity-darkening exponent	⋯	$0.17(\pm 0.3)$	$0.17(\pm 0.3)$
ζ	Stellar oblateness	⋯	0.045 ± 0.007	0.049 ± 0.008

Note. Our rotational splitting measurements yield a high-precision measurement of the stellar rotation rate, but an imprecise constraint of the stellar obliquity because of our low-precision measurements of the star's radius. All of the transit fit results are of lower precision than expected because the companion star is in a grazing configuration, making the constraints of the star's radius and obliquity and the companion's transit geometry nearly degenerate. We apply assumed values for stellar limb-darkening, gravity-darkening, and the transiting object's eccentricity. We use assumed limb-darkening coefficients based on Sing (2010). We estimate KOI-976's gravity-darkening exponent based on previous gravity-darkening works (Monnier et al. 2007; Claret & Bloemen 2011). Due to the grazing nature of the transiting companion, we assume a circular orbit and do not fit eccentricity. The $\chi^2_{\rm red}$ goodness-of-fit for our asteroseismology and short-cadence transit analyses are inflated due to the extremely small photometric uncertainty listed by *Kepler* for the short-cadence data set.

orbital inclination. The projected inclination (closely related to the transit impact parameter) describes how much of the companion actually passes in front of the the star, directly affecting both the transit duration and the transit depth. This effect brings about the large uncertainties seen in Table 2. We display our best estimate of the transit geometry in Figure 5.

Even with all 27 long-cadence transits folded together, KOI-976's single variability-subtracted short-cadence transit provides three times finer precision than its long-cadence counterpart. The standard deviations of the residuals shown in Figure 4 are $\sigma_{\rm SC} = 3 \times 10^{-4}$ and $\sigma_{\rm LC} = 9 \times 10^{-4}$ for the short-cadence and long-cadence best-fit models, respectively, implying that variability subtraction provides a robust path for cleaning transit light curves of stellar seismic activity.

Table 3
Measured Parameters from Rotational Splitting

Parameter	Value
C_{nl}	0.08776 ± 0.00003
D_1	1.97597 ± 0.00013
$\nu_\star (\mu{\rm Hz})$	21.71 ± 0.16
$v \sin(i)$ (km s^{-1})	120 ± 5

Note. We color code the rotational splitting constants according to their multiplet, matching Figure 2. The Ledoux constant falls within the expected range for typical *δ*-Scuti stars. We combine these results and our constraints obtained from transit light curve fitting to measure the star's obliquity angle, which we list in Table 2.

Table 4
The Best-fit Frequencies, Amplitudes, and Phases of 204 Statistically Significant Oscillations in KOI-976's Short-cadence *Kepler* Photometry

#	Freq (μHz)	Amp(10^{-3})	Phase	
1	248.8552 ± 0.0002	2.778 ± 0.005	1.614 ± 0.003	ν_1
2	226.8755 ± 0.0004	1.261 ± 0.010	6.049 ± 0.005	ν_2
3	263.9633 ± 0.0018	1.094 ± 0.004	4.86 ± 0.02	ν_3
4	139.8156 ± 0.0013	0.684 ± 0.006	3.72 ± 0.03	ν_4
5	113.3531 ± 0.0013	0.589 ± 0.006	5.046 ± 0.019	ν_5
6	152.961 ± 0.005	0.444 ± 0.010	2.45 ± 0.06	ν_6
7	137.3857 ± 0.0013	0.375 ± 0.008	6.116 ± 0.016	
8	288.132 ± 0.008	0.2 ± 0.02	3.58 ± 0.08	$2\nu_3 - \nu_6 - 4\nu_\star$
9	228.914 ± 0.006	0.27 ± 0.018	4.71 ± 0.08	
10	130.326 ± 0.005	0.209 ± 0.017	6.00 ± 0.04	$-\nu_4 + 2\nu_5 + 2\nu_\star$
11	174.129 ± 0.005	0.197 ± 0.005	1.19 ± 0.04	$2\nu_2 - 2\nu_4$
12	212.200 ± 0.009	0.17 ± 0.02	1.97 ± 0.05	
13	240.661 ± 0.005	0.15 ± 0.01	2.76 ± 0.04	
14	140.604 ± 0.016	0.148 ± 0.012	5.29 ± 0.10	$-\nu_2 + 2\nu_4 + \nu_6 - 3\nu_\star$
15	289.802 ± 0.004	0.142 ± 0.017	3.14 ± 0.04	
16	125.073 ± 0.006	0.133 ± 0.005	3.87 ± 0.08	$\nu_3 - 2\nu_5 + \nu_6 - 3\nu_\star$
17	179.569 ± 0.009	0.125 ± 0.008	0.34 ± 0.07	$\nu_5 + \nu_6 - 4\nu_\star$
18	268.192 ± 0.003	0.125 ± 0.004	4.02 ± 0.03	$\nu_1 + \nu_3 - \nu_5 - \nu_6 + \nu_\star$
19	258.122 ± 0.004	0.120 ± 0.007	2.1 ± 0.04	
20	134.051 ± 0.005	0.121 ± 0.01	3.81 ± 0.05	
21	270.701 ± 0.006	0.118 ± 0.009	0.17 ± 0.07	
22	152.206 ± 0.010	0.113 ± 0.006	4.9 ± 0.1	$\nu_2 - \nu_4 + 3\nu_\star$
23	95.283 ± 0.006	0.117 ± 0.009	5.57 ± 0.08	$-2\nu_1 + 2\nu_3 + 3\nu_\star$
24	313.581 ± 0.006	0.101 ± 0.006	5.77 ± 0.07	$2\nu_5 + 4\nu_\star$
25	71.53 ± 0.007	0.107 ± 0.007	3.47 ± 0.07	
26	268.626 ± 0.01	0.085 ± 0.009	0.62 ± 0.10	
27	300.480 ± 0.007	0.093 ± 0.010	3.54 ± 0.07	$\nu_2 + \nu_4 - \nu_6 + 4\nu_\star$
28	188.831 ± 0.01	0.091 ± 0.007	3 ± 0.11	
29	236.550 ± 0.005	0.087 ± 0.005	1.96 ± 0.06	$\nu_1 - \nu_2 + 2\nu_4 - 3\nu_\star$
30	219.271 ± 0.010	0.092 ± 0.006	1.16 ± 0.06	
31	310.155 ± 0.009	0.092 ± 0.008	5.96 ± 0.08	$\nu_1 - \nu_5 + \nu_6 + \nu_\star$
32	126.191 ± 0.007	0.088 ± 0.010	4.74 ± 0.06	$\nu_1 + \nu_4 - 2\nu_6 + 2\nu_\star$
33	308.423 ± 0.006	0.08 ± 0.01	1.78 ± 0.06	$2\nu_1 - \nu_3 + \nu_4 - 3\nu_\star$
34	141.167 ± 0.007	0.123 ± 0.008	3.64 ± 0.07	$-\nu_3 + 3\nu_5 + 3\nu_\star$
35	74.95 ± 0.01	0.08 ± 0.01	2.95 ± 0.06	$-\nu_1 - \nu_5 + 3\nu_6 - \nu_\star$
36	200.328 ± 0.009	0.08 ± 0.01	0.36 ± 0.10	$2\nu_3 - 2\nu_6 - \nu_\star$
37	282.288 ± 0.016	0.08 ± 0.01	5.52 ± 0.10	
38	378.185 ± 0.01	0.081 ± 0.008	3.64 ± 0.1	
39	84.462 ± 0.006	0.082 ± 0.008	0.82 ± 0.09	$\nu_3 - \nu_5 - \nu_6 + 4\nu_\star$
40	303.656 ± 0.009	0.078 ± 0.007	5.81 ± 0.09	$2\nu_1 - \nu_3 + \nu_5 - 2\nu_\star$
41	497.713 ± 0.008	0.077 ± 0.008	4.6 ± 0.1	$2\nu_1$
42	286.949 ± 0.008	0.08 ± 0.006	5.11 ± 0.09	
43	231.807 ± 0.013	0.074 ± 0.009	2.31 ± 0.08	$2\nu_2 + \nu_4 - 3\nu_5 - \nu_\star$
44	226.628 ± 0.006	0.074 ± 0.009	3.52 ± 0.1	$\nu_4 + 4\nu_\star$
45	111.685 ± 0.007	0.074 ± 0.008	1.3 ± 0.1	
46	91.013 ± 0.013	0.072 ± 0.007	0.1 ± 0.08	$2\nu_2 - \nu_4 - \nu_5 - \nu_6 + 2\nu_\star$
47	169.236 ± 0.017	0.073 ± 0.009	4.52 ± 0.11	$\nu_2 + 2\nu_3 - 2\nu_4 - 2\nu_6$
48	33.32 ± 0.01	0.088 ± 0.008	5.77 ± 0.08	
49	216.347 ± 0.010	0.07 ± 0.009	3.68 ± 0.09	$\nu_1 - \nu_3 + \nu_4 + \nu_5 - \nu_\star$
50	500.264 ± 0.012	0.064 ± 0.008	0 ± 0.10	
51	12.608 ± 0.005	0.106 ± 0.009	5.48 ± 0.06	$2\nu_2 - 3\nu_4 - \nu_\star$
52	14.284 ± 0.010	0.117 ± 0.013	3.93 ± 0.07	
53	21.705 ± 0.009	0.069 ± 0.013	3.83 ± 0.1	$\nu_\star$
54	26.074 ± 0.008	0.072 ± 0.010	4.6 ± 0.09	$-\nu_1 + 3\nu_5 - 3\nu_\star$
55	76.653 ± 0.009	0.058 ± 0.009	2.62 ± 0.1	
56	173.513 ± 0.012	0.06 ± 0.009	4.16 ± 0.14	
57	150.403 ± 0.013	0.06 ± 0.006	3.91 ± 0.11	$\nu_3 - 3\nu_4 + 2\nu_6$
58	154.897 ± 0.010	0.061 ± 0.009	5.70 ± 0.1	$\nu_1 + \nu_3 - \nu_4 - \nu_6 - 3\nu_\star$
59	127.347 ± 0.010	0.065 ± 0.008	1.96 ± 0.10	$\nu_4 - 3\nu_5 + 2\nu_6 + \nu_\star$
60	127.62 ± 0.02	0.03 ± 0.007	1.4 ± 0.3	
61	162.348 ± 0.013	0.06 ± 0.010	2.93 ± 0.13	$-\nu_2 + 2\nu_4 + \nu_6 - 2\nu_\star$
62	69.754 ± 0.010	0.055 ± 0.006	4.83 ± 0.14	$2\nu_3 - \nu_4 - 3\nu_5 + \nu_\star$
63	43.429 ± 0.016	0.049 ± 0.007	5.53 ± 0.17	$2\nu_\star$
64	143.277 ± 0.010	0.052 ± 0.008	1.5 ± 0.16	

Table 4
(Continued)

#	Freq (μHz)	Amp(10^{-3})	Phase	
65	89.819 ± 0.010	0.053 ± 0.008	3.04 ± 0.17	$-\nu_1 + \nu_3 + \nu_4 - 3\nu_\star$
66	23.487 ± 0.014	0.053 ± 0.009	1.09 ± 0.13	$2\nu_2 - \nu_3 - 2\nu_4 + \nu_5$
67	229.079 ± 0.008	0.069 ± 0.009	5.61 ± 0.09	$-\nu_1 - 2\nu_2 + 3\nu_3 + \nu_4$
68	305.959 ± 0.013	0.05 ± 0.01	2.56 ± 0.17	$2\nu_6$
69	338.033 ± 0.014	0.048 ± 0.009	0.8 ± 0.2	$-\nu_1 + 3\nu_3 - 2\nu_5 + \nu_\star$
70	118.085 ± 0.016	0.048 ± 0.009	5.87 ± 0.17	$\nu_4 - \nu_\star$
71	313.983 ± 0.017	0.052 ± 0.008	1.93 ± 0.11	$\nu_1 + 3\nu_\star$
72	294.120 ± 0.013	0.052 ± 0.007	4.95 ± 0.19	
73	78.362 ± 0.017	0.049 ± 0.008	1.70 ± 0.14	$-2\nu_4 + 2\nu_5 + \nu_6 - \nu_\star$
74	289.055 ± 0.016	0.063 ± 0.007	3.53 ± 0.08	
75	308.809 ± 0.010	0.05 ± 0.007	5.65 ± 0.17	
76	187.117 ± 0.014	0.04 ± 0.01	6.1 ± 0.19	$3\nu_5 - \nu_6$
77	109.331 ± 0.014	0.045 ± 0.009	0.04 ± 0.17	$-\nu_2 + \nu_4 + \nu_6 + 2\nu_\star$
78	100.192 ± 0.014	0.045 ± 0.008	1.06 ± 0.16	$\nu_4 + \nu_5 - \nu_6$
79	332.09 ± 0.02	0.04 ± 0.01	1.31 ± 0.13	$\nu_1 + 2\nu_4 - \nu_6 - 2\nu_\star$
80	293.430 ± 0.016	0.042 ± 0.008	2.97 ± 0.16	
81	337.362 ± 0.019	0.044 ± 0.008	6.21 ± 0.17	
82	12.009 ± 0.014	0.063 ± 0.010	4.21 ± 0.11	
83	28.812 ± 0.012	0.046 ± 0.006	4.91 ± 0.11	$-\nu_3 + \nu_4 + \nu_6$
84	42.061 ± 0.017	0.043 ± 0.013	4.4 ± 0.3	
85	254.633 ± 0.017	0.046 ± 0.007	0.67 ± 0.17	$\nu_3 + \nu_4 + \nu_5 - 2\nu_6 + 2\nu_\star$
86	195.270 ± 0.013	0.046 ± 0.01	5.5 ± 0.2	
87	264.447 ± 0.017	0.042 ± 0.008	4.52 ± 0.19	$\nu_1 + \nu_3 - 2\nu_5 - \nu_\star$
88	129.350 ± 0.010	0.051 ± 0.010	3.41 ± 0.17	$\nu_1 + \nu_3 - 3\nu_5 - 2\nu_\star$
89	251.282 ± 0.014	0.043 ± 0.009	2.66 ± 0.19	$\nu_1 + \nu_3 + \nu_4 - 2\nu_5 - \nu_6 - \nu_\star$
90	165.52 ± 0.03	0.022 ± 0.005	1.7 ± 0.4	$\nu_2 + \nu_5 - \nu_6 - \nu_\star$
91	165.61 ± 0.03	0.025 ± 0.007	0.9 ± 0.4	$\nu_2 + \nu_5 - \nu_6 - \nu_\star$
92	111.025 ± 0.014	0.043 ± 0.008	4.98 ± 0.2	$\nu_3 - \nu_6$
93	91.454 ± 0.017	0.042 ± 0.008	1.2 ± 0.2	$-\nu_2 + 3\nu_5 - \nu_\star$
94	49.00 ± 0.02	0.043 ± 0.006	2.02 ± 0.14	$-\nu_2 + 2\nu_4 - \nu_5 + \nu_6 - 2\nu_\star$
95	271.836 ± 0.017	0.04 ± 0.007	5.5 ± 0.3	$\nu_2 + \nu_3 - \nu_4 + 2\nu_5 - 2\nu_6$
96	156.11 ± 0.02	0.039 ± 0.007	4.96 ± 0.2	$\nu_2 + 2\nu_3 - \nu_4 - 3\nu_6$
97	183.28 ± 0.02	0.04 ± 0.01	5.6 ± 0.2	$2\nu_5 - 2\nu_\star$
98	203.639 ± 0.02	0.041 ± 0.008	5.28 ± 0.17	$\nu_3 + \nu_4 - \nu_5 - 4\nu_\star$
99	72.21 ± 0.03	0.036 ± 0.009	6.2 ± 0.2	$2\nu_1 - \nu_3 - \nu_4 - \nu_\star$
100	49.749 ± 0.013	0.041 ± 0.006	4.2 ± 0.2	$\nu_2 - \nu_3 + 4\nu_\star$
101	327.468 ± 0.019	0.039 ± 0.008	3.7 ± 0.2	$-\nu_2 + 2\nu_5 + 2\nu_6 + \nu_\star$
102	326.98 ± 0.03	0.038 ± 0.008	4.1 ± 0.2	$\nu_4 + 3\nu_5 - \nu_6$
103	93.402 ± 0.019	0.042 ± 0.009	3.3 ± 0.2	$\nu_1 + \nu_3 - 3\nu_4$
104	93.21 ± 0.02	0.026 ± 0.008	3.1 ± 0.4	$\nu_2 - \nu_3 - \nu_4 + 2\nu_5 + 2\nu_\star$
105	92.68 ± 0.02	0.041 ± 0.010	3.76 ± 0.16	$\nu_4 - \nu_5 + \nu_6 - 4\nu_\star$
106	290.41 ± 0.05	0.043 ± 0.008	3.27 ± 0.14	$\nu_3 + \nu_4 - \nu_5$
107	314.423 ± 0.016	0.041 ± 0.006	3.1 ± 0.2	$2\nu_1 - 2\nu_5 + 2\nu_\star$
108	248.670 ± 0.014	0.03 ± 0.01	5 ± 0.3	$\nu_1 - \nu_2 + 2\nu_5$
109	311.435 ± 0.019	0.043 ± 0.008	1.15 ± 0.16	$\nu_2 + \nu_3 - \nu_4 + \nu_5 - \nu_6$
110	165.925 ± 0.013	0.042 ± 0.009	5 ± 0.2	$-\nu_2 + 2\nu_6 + 4\nu_\star$
111	253.663 ± 0.017	0.038 ± 0.008	0.6 ± 0.2	$2\nu_2 - \nu_5 - 4\nu_\star$
112	294.706 ± 0.016	0.041 ± 0.009	3.4 ± 0.2	$-2\nu_2 + 3\nu_3 - 2\nu_\star$
113	163.78 ± 0.02	0.039 ± 0.009	0.7 ± 0.2	$2\nu_1 - \nu_3 - \nu_5 + 2\nu_\star$
114	120.908 ± 0.02	0.041 ± 0.008	4.13 ± 0.19	$\nu_1 - \nu_3 + \nu_4 - \nu_5 + \nu_6 - 2\nu_\star$
115	236.78 ± 0.02	0.034 ± 0.008	4.2 ± 0.2	$-\nu_2 + \nu_4 - \nu_5 + 3\nu_6 - \nu_\star$
116	170.47 ± 0.03	0.038 ± 0.009	1.6 ± 0.2	$-\nu_1 + \nu_5 + 2\nu_6$
117	239.813 ± 0.016	0.036 ± 0.008	2.9 ± 0.3	$\nu_6 + 4\nu_\star$
118	272.67 ± 0.03	0.033 ± 0.008	2 ± 0.2	$-\nu_1 - \nu_2 + 3\nu_3 - 2\nu_\star$
119	313.254 ± 0.017	0.04 ± 0.008	2.7 ± 0.2	
120	401.797 ± 0.017	0.039 ± 0.008	0.29 ± 0.19	$\nu_1 + \nu_6$
121	42.553 ± 0.018	0.04 ± 0.009	2.4 ± 0.2	$2\nu_3 - \nu_4 + \nu_5 - 3\nu_6$
122	25.576 ± 0.013	0.039 ± 0.008	5.21 ± 0.19	$-\nu_4 + 3\nu_5 - \nu_6 - \nu_\star$
123	28.24 ± 0.02	0.036 ± 0.006	5.58 ± 0.19	$-\nu_1 + \nu_3 - \nu_4 + \nu_6$
124	24.32 ± 0.03	0.036 ± 0.012	1.5 ± 0.2	$\nu_1 - \nu_2 - \nu_3 + \nu_5 + \nu_6$
125	238.96 ± 0.04	0.033 ± 0.009	3.3 ± 0.2	
126	47.66 ± 0.02	0.03 ± 0.01	3.51 ± 0.2	$\nu_2 + 2\nu_4 - 3\nu_6$
127	68.073 ± 0.014	0.039 ± 0.008	3.4 ± 0.3	$-\nu_1 + \nu_3 + \nu_4 - 4\nu_\star$
128	289.403 ± 0.019	0.043 ± 0.009	4.09 ± 0.17	$\nu_3 + \nu_5 - \nu_6 + 3\nu_\star$

Table 4
(Continued)

#	Freq (μHz)	Amp(10^{-3})	Phase	
129	270.149 ± 0.018	0.032 ± 0.006	6.2 ± 0.3	$2\nu_5 + 2\nu_\star$
130	332.95 ± 0.02	0.035 ± 0.008	0.3 ± 0.2	$3\nu_3 - 3\nu_6$
131	202.43 ± 0.02	0.033 ± 0.008	4.1 ± 0.2	$\nu_3 - 2\nu_4 + \nu_6 + 3\nu_\star$
132	31.673 ± 0.019	0.033 ± 0.008	1.1 ± 0.3	
133	185.22 ± 0.02	0.033 ± 0.007	3.3 ± 0.2	$\nu_1 + \nu_3 - 2\nu_6 - \nu_\star$
134	198.58 ± 0.03	0.034 ± 0.009	3.33 ± 0.2	$-\nu_2 + \nu_3 + \nu_4 + \nu_\star$
135	286.26 ± 0.03	0.031 ± 0.009	1.51 ± 0.2	$\nu_1 - \nu_3 + 2\nu_4 + \nu_\star$
136	137.145 ± 0.017	0.031 ± 0.009	2.7 ± 0.3	$-\nu_2 + \nu_3 - 2\nu_4 + 2\nu_5 + \nu_6$
137	182.74 ± 0.02	0.035 ± 0.008	1.6 ± 0.3	$\nu_1 - \nu_6 + 4\nu_\star$
138	312.192 ± 0.02	0.031 ± 0.007	1.6 ± 0.3	$\nu_3 + \nu_5 - 3\nu_\star$
139	217.84 ± 0.02	0.029 ± 0.007	6 ± 0.3	$\nu_1 + \nu_2 - 2\nu_4 + \nu_\star$
140	84.76 ± 0.02	0.032 ± 0.008	2 ± 0.2	$\nu_3 + 2\nu_4 - 3\nu_6$
141	395.06 ± 0.02	0.032 ± 0.008	5.3 ± 0.2	$\nu_1 + \nu_2 - \nu_3 + 2\nu_5 - 2\nu_\star$
142	148.59 ± 0.03	0.033 ± 0.009	2.5 ± 0.3	$-2\nu_1 + \nu_2 + 3\nu_4$
143	193.90 ± 0.03	0.031 ± 0.008	5 ± 0.3	$-\nu_2 + \nu_3 + \nu_5 + 2\nu_\star$
144	192.95 ± 0.02	0.032 ± 0.008	5.5 ± 0.2	
145	166.96 ± 0.03	0.034 ± 0.009	3.18 ± 0.2	$-\nu_2 + 3\nu_6 - 3\nu_\star$
146	38.34 ± 0.02	0.035 ± 0.009	3.5 ± 0.2	$2\nu_2 - 3\nu_6 + 2\nu_\star$
147	197.866 ± 0.014	0.034 ± 0.009	5.3 ± 0.3	$\nu_3 - \nu_6 + 4\nu_\star$
148	67.21 ± 0.03	0.031 ± 0.008	3.58 ± 0.19	
149	364.973 ± 0.019	0.031 ± 0.008	3 ± 0.3	$\nu_1 - 2\nu_2 + \nu_3 + 2\nu_6$
150	287.403 ± 0.013	0.043 ± 0.008	1.21 ± 0.17	$2\nu_1 + \nu_2 - 3\nu_6 + \nu_\star$
151	79.76 ± 0.02	0.029 ± 0.007	1.9 ± 0.3	$\nu_3 - 2\nu_4 + 2\nu_5 - \nu_6 + \nu_\star$
152	211.260 ± 0.014	0.032 ± 0.008	5.9 ± 0.3	$-\nu_1 + 3\nu_2 - \nu_3 + 2\nu_\star$
153	72.78 ± 0.02	0.029 ± 0.007	4.2 ± 0.3	$\nu_1 - \nu_3 + \nu_6 - 3\nu_\star$
154	273.223 ± 0.019	0.03 ± 0.009	0.5 ± 0.4	$2\nu_1 - \nu_2 - \nu_3 + \nu_5 + \nu_6$
155	86.73 ± 0.02	0.03 ± 0.008	4.1 ± 0.3	$4\nu_\star$
156	228.637 ± 0.012	0.034 ± 0.008	5.9 ± 0.3	
157	335.35 ± 0.02	0.03 ± 0.008	1 ± 0.3	$\nu_2 + 2\nu_3 - 3\nu_4$
158	204.75 ± 0.03	0.031 ± 0.008	4.7 ± 0.3	$-\nu_1 + \nu_2 + 2\nu_5$
159	61.35 ± 0.02	0.032 ± 0.008	5.2 ± 0.3	$-\nu_5 + \nu_6 + \nu_\star$
160	298.78 ± 0.03	0.03 ± 0.008	3.3 ± 0.3	$2\nu_1 - \nu_3 + 3\nu_\star$
161	287.908 ± 0.014	0.04 ± 0.012	0.1 ± 0.3	
162	292.95 ± 0.02	0.03 ± 0.009	5.1 ± 0.3	$3\nu_1 - \nu_2 - 2\nu_5$
163	284.25 ± 0.02	0.029 ± 0.008	2.4 ± 0.2	$2\nu_6 - \nu_\star$
164	249.110 ± 0.018	0.032 ± 0.008	3.8 ± 0.3	$2\nu_1 - \nu_2 - \nu_\star$
165	51.09 ± 0.03	0.03 ± 0.008	2.3 ± 0.3	$\nu_1 - \nu_3 + \nu_6 - 4\nu_\star$
166	52.63 ± 0.02	0.029 ± 0.008	1.8 ± 0.3	$-\nu_2 + 2\nu_3 - 2\nu_5 - \nu_\star$
167	22 ± 0.03	0.028 ± 0.008	2.9 ± 0.3	$\nu_1 - \nu_2$
168	255.43 ± 0.04	0.026 ± 0.008	2.5 ± 0.3	$2\nu_1 - \nu_3 + \nu_\star$
169	88.646 ± 0.02	0.031 ± 0.008	2.2 ± 0.3	
170	153.45 ± 0.03	0.029 ± 0.009	2.2 ± 0.3	$\nu_1 - 2\nu_5 + \nu_6 - \nu_\star$
171	401.42 ± 0.03	0.025 ± 0.007	3.2 ± 0.4	$2\nu_5 + \nu_6 + \nu_\star$
172	280.06 ± 0.04	0.025 ± 0.008	4.4 ± 0.4	$\nu_1 + 2\nu_4 - 2\nu_5 - \nu_\star$
173	188.12 ± 0.02	0.028 ± 0.008	6 ± 0.3	$\nu_4 + \nu_5 - 3\nu_\star$
174	266.31 ± 0.03	0.026 ± 0.009	0 ± 0.3	$\nu_5 + \nu_6$
175	301.43 ± 0.03	0.026 ± 0.008	3.1 ± 0.3	$\nu_4 + 2\nu_5 - 3\nu_\star$
176	10.194 ± 0.019	0.04 ± 0.006	2.29 ± 0.16	
177	13.483 ± 0.014	0.043 ± 0.007	5.8 ± 0.2	$3\nu_1 - \nu_2 - 2\nu_3 + \nu_\star$
178	30.285 ± 0.018	0.035 ± 0.009	0.2 ± 0.3	$\nu_4 - \nu_6 + 2\nu_\star$
179	21.4 ± 0.02	0.038 ± 0.007	2 ± 0.17	$-\nu_1 + \nu_2 + 2\nu_\star$
180	17.33 ± 0.02	0.036 ± 0.010	1.18 ± 0.17	
181	17.74 ± 0.03	0.033 ± 0.009	5.3 ± 0.2	$-3\nu_4 + 3\nu_6 - \nu_\star$
182	27.15 ± 0.02	0.038 ± 0.009	3.2 ± 0.2	$\nu_1 - 3\nu_2 + 3\nu_6$
183	16.10 ± 0.04	0.025 ± 0.007	4 ± 0.3	$\nu_1 - \nu_3 + 2\nu_4 - 2\nu_5 - \nu_\star$
184	258.35 ± 0.02	0.03 ± 0.007	3.8 ± 0.3	
185	1.153 ± 0.006	0.31 ± 0.03	5.00 ± 0.09	
186	9.266 ± 0.008	0.119 ± 0.016	2.81 ± 0.08	$-3\nu_5 + 2\nu_6 + 2\nu_\star$
187	1.880 ± 0.003	0.20 ± 0.02	3.70 ± 0.03	
188	0.23 ± 0.14	0.197 ± 0.008	3.923 ± 0.003	
189	3.621 ± 0.008	0.171 ± 0.016	2.49 ± 0.08	$-\nu_2 + 3\nu_5 - \nu_6 + 2\nu_\star$
190	2.188 ± 0.003	0.144 ± 0.019	4.75 ± 0.06	$-\nu_2 - \nu_3 + 3\nu_5 + \nu_6$
191	3.898 ± 0.012	0.062 ± 0.014	0.74 ± 0.10	$-\nu_4 + 3\nu_5 - \nu_6 - 2\nu_\star$
192	211.962 ± 0.014	0.044 ± 0.007	4.2 ± 0.17	$\nu_3 - \nu_4 + \nu_6 - 3\nu_\star$

Table 4
(Continued)

#	Freq (μHz)	Amp(10^{-3})	Phase	
193	6.81 ± 0.014	0.043 ± 0.007	1.6 ± 0.2	$-\nu_2 + \nu_3 - \nu_4 + \nu_6 - 2\nu_\star$
194	2.97 ± 0.014	0.056 ± 0.008	4.6 ± 0.07	$-\nu_2 + \nu_3 - 3\nu_5 + 2\nu_6$
195	288.790 ± 0.018	0.04 ± 0.008	3.2 ± 0.2	$-\nu_2 + \nu_4 + \nu_5 + 2\nu_6 - 2\nu_\star$
196	1.205 ± 0.006	0.04 ± 0.006	0.75 ± 0.05	
197	130.063 ± 0.019	0.036 ± 0.008	2.4 ± 0.2	$\nu_1 + 3\nu_5 - 3\nu_6$
198	268.76 ± 0.02	0.036 ± 0.008	4.6 ± 0.2	$\nu_3 + \nu_4 - \nu_5 - \nu_\star$
199	7.19 ± 0.03	0.036 ± 0.007	4.69 ± 0.17	$3\nu_1 - 2\nu_2 - \nu_3 - \nu_\star$
200	174.33 ± 0.02	0.032 ± 0.008	2.4 ± 0.3	$3\nu_1 - \nu_5 - 3\nu_6$
201	23.8 ± 0.02	0.033 ± 0.008	3.7 ± 0.2	
202	137.53 ± 0.02	0.032 ± 0.009	1.2 ± 0.3	$\nu_3 + \nu_5 - \nu_6 - 4\nu_\star$
203	12.81 ± 0.02	0.032 ± 0.007	2.6 ± 0.2	$2\nu_2 - \nu_5 - 2\nu_6 - \nu_\star$
204	8.522 ± 0.017	0.032 ± 0.007	5.7 ± 0.3	$-2\nu_1 + 2\nu_3 - \nu_\star$

Note. We subtract each oscillation using the Linear Algorithm for Significance Reduction (LASR) and calculate uncertainties following Ahlers et al. (2018). We also identify possible combination frequencies of the six highest amplitude frequencies and the rotation frequency. We find that 160 out of 204 total oscillations match combination values of KOI-976's dominant modes of oscillation and identified rotation frequency. All predicted combinations are within 1σ of their observed values, with the average uncertainty of all combinations below 0.5σ.
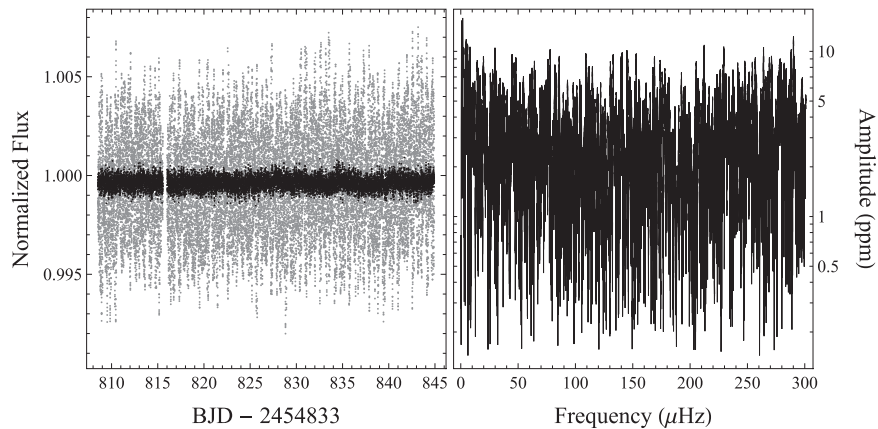
Figure 3. Left: original (gray) and subtracted (black) Q9 short-cadence photometry. We subtract off the 204 frequencies listed in Table 4 to clean the time series and prepare it for transit light curve analysis. The data gap near 815 days is the transit event, which we mask out of the data set during the variability-subtraction process. We extend our subtraction results through the transit event to remove variability (see Figure 1). Right: KOI-976's frequency power spectrum after subtracting all identified modes of oscillation.

4. Discussion

This work tests the feasibility of a combined asteroseismic and transit light curve analysis of planets transiting high-mass variable stars. NASA's *TESS* mission will likely discover over a thousand exoplanets orbiting rapidly rotating stars, and as many as a few hundred of them will orbit δ-Scuti or related variable stars (Barclay et al. 2018). We demonstrate that the obstacles of rapid rotation and variability can be overcome and even used advantageously during transit light curve analysis.

Asteroseismology can provide a wealth of information about host stars. We only skim the surface of asteroseismology's capabilities in this work by applying rotational splitting theory to measure the host star's external rotation rate and obliquity angle. δ-Scuti possess the fortuitous characteristic of typically being dominated by a few low-order modes of oscillation, making rotational splitting an accessible form of analysis. We identify a frequency triplet in Figure 2 that dominates the variability seen in KOI-976's *Kepler* photometry. We find that the triplet displays asymmetric rotational splitting consistent with rapid stellar rotation and identify the star's rotation in its frequency power spectrum following previous works on δ-Scuti (e.g., Breger 2000; Breger et al. 2011).

Our results demonstrate that variability subtraction for δ-Scuti and related variable stars provides a reliable process for making transit light curve analysis possible. Using the variability removal program LASR (Ahlers et al. 2018), we show that the single short-cadence transit event can provide superior photometric precision to removing variability by phase-folding.

We find that this system resides in a spin–orbit misaligned configuration. Our asteroseismic and light curve fitting procedures measure the host star's obliquity rate to be $42° \pm 10°$ when treating the three approaches as three independent measurements. Exoplanets (and binary companions) orbiting high-mass stars ($M_\star \gtrsim 1.3\,M_\odot$) are expected to reside in misaligned orbits far more commonly than for those orbiting low-mass stars, so our results are consistent with other works on spin–orbit misalignment (Winn et al. 2010; Albrecht et al. 2012; Dawson 2014).

4.1. δ-Scuti Stars and TESS

We choose KOI-976 as our example system for this work because this star is a prototypical rapidly rotating δ-Scuti and because of its exceptional signal-to-noise. However, *TESS*
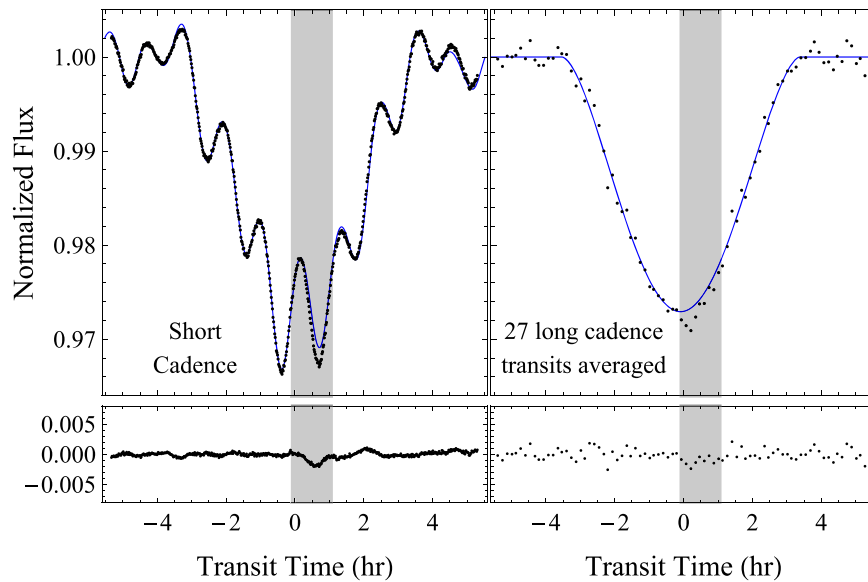
Figure 4. KOI-976 short-cadence (left) and long-cadence (right) *Kepler* transit light curves and best-fit models. The short-cadence best-fit model includes both the gravity-darkened fit and the 204 oscillation modes resolved in the data set. The long-cadence light curve includes 27 phase-folded transits and is binned to average out stellar variability. The gaps in the data sets and their residuals correspond to masking out the transit analomaly (see Figure 1). The short-cadence approach of variability subtraction yields a slightly better overall fit than averaging out variability through phase-folding with residual standard deviations of $\sigma_{SC} = 3 \times 10^{-4}$ and $\sigma_{LC} = 9 \times 10^{-4}$.
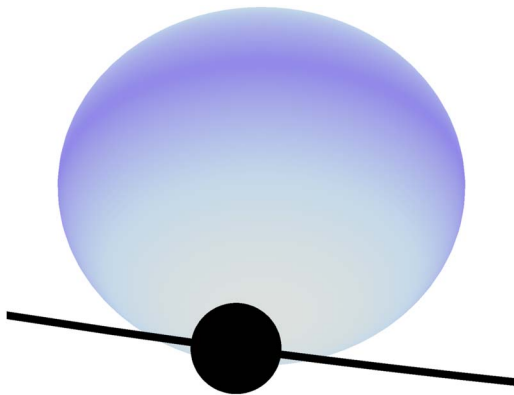
Figure 5. Our best estimate of KOI-976's transit geometry. We find that the companion star transits near one of the primary star's brighter poles in a grazing configuration. The transit of our results contains a high uncertainty for the transit geometry due to its grazing nature, but asteroseismic analysis provides a reliable obliquity value for the primary star.

photometry will not achieve the same precision as *Kepler*; with an effective aperture size of 10 cm (Ricker et al. 2014), *TESS* will only obtain approximately one hundredth the precision of its predecessor. Therefore future transit light curve analyses of rapidly rotating δ-Scuti will likely not involve such detailed resolution of stellar variability or of transit events.

The gravity-darkening technique will still apply for low-signal photometry. Barnes et al. (2015) demonstrated that gravity-darkening can still make constraints on a planet's orbit geometry even when a transit event is barely visible. Similarly, gravity-darkening can provide upper limits on the projected alignment of *TESS* objects orbiting rapid rotators based on the gravity-darkening-induced asymmetry (or lack thereof) in their transit light curves.

Detection of rotational splitting is also possible from low-precision photometry. δ-Scuti stars are typically dominated by a few low-order modes, making multiplets often easy to identify in frequency space. For rapid rotators, multiplets split apart by

several tens of μHz, making them easy to resolve in frequency space even with low-precision data and with only 27 days of baseline photometry. Ahlers et al. (2018) show that oscillations can be reliably measured when their amplitudes are as little as one-tenth of the data's noise level.

Variability subtraction will be particularly useful for *TESS* systems. Section 3.3 shows that variability subtraction yields a better result than phase-folding transits even with 27 available transit events to average out the seismic signal. Most *TESS* systems will only have one or a few transits available, so phase-folding to average out variability such as KOI-976's will not be viable. Variability subtraction will be the most viable method of overcoming stellar variability during the *TESS* era.

4.2. Transit Anomaly

The transit anomaly shown in Figure 1 is a sharp, ∼1 hr drop in brightness approximately 60% of the way through the transit. This signal appears in the short-cadence transit light curve after stellar variability has been subtracted and appears in each of KOI-976's 27 individual long-cadence transits. The dimming event also appears in the phase-folded version of the long-cadence transit. We therefore suspect that the anomaly is astrophysical and not a systematic in our data set because the event occurs periodically in the same part of KOI-976's transit events with the same basic shape, duration, and depth, and appears in both short-cadence and long-cadence photometry.

Detailed analysis of the unusual signal is outside the scope of this work, however we rule out many possibilities through simple thought exercises. Many events can cause a decrease in photometric brightness, but no straightforward phenomena match the observed signal.

The existence of an additional transiting body likely cannot explain the short, sudden decrease in brightness shown in Figure 1. The anomaly occurs every transit, so an object with one-half the binary companion's orbit period could cause a signal in sync with every primary transit event. The anomaly's signal in variability-subtracted short-cadence photometry is 2σ

larger than the out-of-transit baseline noise, but we find no evidence of the anomaly occurring outside of the transit event.

Rings or an accretion disk around the transiting body also cannot produce the anomaly. Barnes & Fortney (2004) and others (Kenworthy & Mamajek 2015; des Etangs et al. 2017; Aizawa et al. 2018; Hatchett et al. 2018) model the possible photometric signals a ring system or accretion disk can produce during a transit/eclipse. Most prominent in transits with rings is an increased effective radius of the transiting body and distinct jumps upward in the light curve due to light passing through gaps in the rings. Rings/accretion disks do not match the anomalous signal in Figure 1 and can be ruled out.

The anomaly displays the exact opposite characteristics of a transit across a starspot. Rather than a short-lived increase in photometric signal as seen with stroboscopic starspots (e.g., Désert et al. 2011; Sanchis-Ojeda et al. 2011), we see a distinct drop in brightness as if the transiting companion were passing in front of a local hot spot on the primary star. Stellar hot spots have been observed in the past that were likely brought about by instabilities in the star's magnetic field, but only for T Tauri stars (Kenyon et al. 1994). No prior observations indicate that a main-sequence star variable can possess local hot spots on their surface. The anomaly appears at the same time in every transit event, so if it is caused by a hot spot or some other form of local instability and must not be affected by the star's rotation rate. The hot spot would therefore need to be located at one of the host star's poles, which is consistent with our transit geometry. However, validation of the hot spot hypothesis for this transit signal is outside the scope of this work.

5. Conclusion

The gravity-darkening, rotational splitting, and variability-subtraction techniques described in this manuscript provide new windows for studying planets and binary companions orbiting high-mass stars. A/F-type stars commonly exhibit rapid rotation and stellar variability that can obfuscate detailed analysis of transit photometry. We demonstrate how to overcome these challenges and use them to constrain the transiting body's orbit geometry.

Exoplanets orbiting high-mass stars such as KOI-976 commonly reside in spin–orbit misaligned positions (Winn et al. 2010). While the underlying mechanisms for causing misalignment are still under investigation, recent observations have found many high-mass stars to host severely inclined or even retrograde planets (e.g., Barnes et al. 2011; Winn et al. 2011; Albrecht et al. 2012; Ahlers et al. 2015; Gaudi et al. 2017).

With better constraints on the distribution of alignment angles around high-mass stars, the dominant mechanisms for causing exoplanets to misalign will become clearer. Measuring bulk parameters and orbit geometries of systems such as KOI-976 helps constrain the formation and evolution pathways of such systems and helps explain the apparent dichotomy between high-mass and low-mass system geometries.

This work demonstrates one approach to measuring system parameters around active, rapidly rotating high-mass stars that applies well to NASA's *TESS* mission. With a spectro-scopically determined $v \sin(i)$ value for the host star, one can potentially obtain two independent measurements of a transiting body's orbit geometry directly from *TESS* photometry using asteroseismology and gravity-darkening. The techniques

detailed in this manuscript will likely apply to as many as several hundred *TESS* systems in the near future.

ORCID iDs

Jason W. Barnes ⓘ https://orcid.org/0000-0002-7755-3530

References

Aerts, C., Christensen-Dalsgaard, J., & Kurtz, D. W. 2010, Asteroseismology (New York: Springer)
Ahlers, J. P. 2016, ApJ, 832, 93
Ahlers, J. P., Barnes, J. W., & Barnes, R. 2015, ApJ, 814, 67
Ahlers, J. P., Barnes, J. W., Horvath, S. A., Myers, S. A., & Hedman, M. M. 2018, A&A, 615, A128
Ahlers, J. P., Seubert, S. A., & Barnes, J. W. 2014, ApJ, 786, 131
Aizawa, M., Masuda, K., Kawahara, H., & Suto, Y. 2018, AJ, 155, 206
Albrecht, S., Winn, J. N., Johnson, J. A., et al. 2012, ApJ, 757, 18
Bagnulo, S., Landstreet, J., Mason, E., et al. 2006, A&A, 450, 777
Ballot, J., Lignières, F., Reese, D., & Rieutord, M. 2010, A&A, 518, A30
Balona, L. 2014, MNRAS, 443, 1946
Balona, L., & Nemec, J. 2012, MNRAS, 426, 2413
Baranec, C., Ziegler, C., Law, N. M., et al. 2016, AJ, 152, 18
Barclay, T., Pepper, J., & Quintana, E. V. 2018, ApJS, 239, 2
Barnes, J. W. 2007, PASP, 119, 986
Barnes, J. W. 2009, ApJ, 705, 683
Barnes, J. W., Ahlers, J. P., Seubert, S. A., & Relles, H. M. 2015, ApJL, 808, L38
Barnes, J. W., & Fortney, J. J. 2004, ApJ, 616, 1193
Barnes, J. W., Linscott, E., & Shporer, A. 2011, ApJS, 197, 10
Boehm, T., Holschneider, M., Lignières, F., et al. 2015, A&A, 577, A64
Breger, M. 2000, in ASP Conf. Ser. 210, Delta Scuti and Related Stars, ed. M. Breger & M. Montgomery (San Fransisco, CA: ASP), 3
Breger, M. 2011, in Carnegie Observatory Astrophysics Ser. 5, RR Lyrae Stars, Metal-Poor Stars, and the Galaxy, ed. A. McWilliam (Pasadena, CA: The Observatories of the Carnegie Institution of Washington), 66
Breger, M. 2016, A&A, 592, A97
Breger, M., Balona, L., Lenz, P., et al. 2011, MNRAS, 414, 1721
Burke, K., Reese, D., & Thompson, M. 2011, MNRAS, 414, 1119
Campante, T., Lund, M., Kuszlewicz, J. S., et al. 2016, ApJ, 819, 85
Chaplin, W., Sanchis-Ojeda, R., Campante, T., et al. 2013, ApJ, 766, 101
Charbonneau, P. 2014, ARA&A, 52, 251
Claret, A., & Bloemen, S. 2011, A&A, 529, A75
Dawson, R. I. 2014, ApJL, 790, L31
Demircan, O., & Kahraman, G. 1991, Ap&SS, 181, 313
de Mooij, E., Brogi, M., de Kok, R., et al. 2013, A&A, 550, A54
Désert, J.-M., Charbonneau, D., Demory, B.-O., et al. 2011, ApJS, 197, 14
des Etangs, A. L., Hébrard, G., Blandin, S., et al. 2017, A&A, 603, A115
Deupree, R. G. 1990, ApJ, 357, 175
Deupree, R. G., & Beslin, W. 2010, ApJ, 721, 1900
Dziembowski, W., & Goode, P. R. 1992, ApJ, 394, 670
Gaudi, B. S., Stassun, K. G., Collins, K. A., et al. 2017, Natur, 546, 514
Goupil, M.-J., Dziembowski, W., Pamyatnykh, A., & Talon, S. 2000, in ASP Conf. Ser. 210, Delta Scuti and Related Stars, ed. M. Breger & M. Montgomery (San Fransisco, CA: ASP), 267
Hansen, C. J., & Kawaler, S. D. 1994, Stellar Interiors. Physical Principles, Structure, and Evolution (New York: Springer)
Hatchett, W. T., Barnes, J. W., Ahlers, J. P., MacKenzie, S. M., & Hedman, M. M. 2018, NewA, 60, 88
Herrero, E., Morales, J. C., Ribas, I., & Naves, R. 2011, A&A, 526, L10
Huang, W., & Gies, D. R. 2006, ApJ, 648, 580
Huber, D., Carter, J. A., Barbieri, M., et al. 2013, Sci, 342, 331
Jackson, S., MacGregor, K. B., & Skumanich, A. 2004, ApJ, 606, 1196
Kamiaka, S., Benomar, O., Suto, Y., et al. 2019, AJ, 157, 137
Kenworthy, M. A., & Mamajek, E. E. 2015, ApJ, 800, 126
Kenyon, S., Hartmann, L., Hewett, R., et al. 1994, AJ, 107, 2153
Kervella, P., Jankov, S., Vakili, F., et al. 2005, A&A, 442, 567
Lignières, F., Rieutord, M., & Reese, D. 2006, A&A, 455, 607
Machado, L. F., Michel, R., Álvarez, M., et al. 2008, CoAst, 153, 20
Meibom, S., Mathieu, R. D., & Stassun, K. G. 2009, ApJ, 695, 679
Mestel, L. 1968, MNRAS, 138, 359
Monnier, J. D., Zhao, M., Pedretti, E., et al. 2007, Sci, 317, 342
Murphy, S. J., Shibahashi, H., & Kurtz, D. W. 2013, MNRAS, 430, 2986
Ouazzani, R.-M., Dupret, M.-A., & Reese, D. 2012, A&A, 547, A75

Pigulski, A., Kolaczkowski, Z., Ramza, T., & Narwid, A. 2006, MmSAI, 77, 223

Reese, D., Lignières, F., & Rieutord, M. 2006, A&A, 455, 621

Ricker, G. R., Winn, J. N., Vanderspek, R., et al. 2014, JATIS, 1, 014003

Royer, F., Grenier, S., Baylac, M., Gómez, A., & Zorec, J. 2002, A&A, 393, 897

Sanchis-Ojeda, R., Winn, J. N., Holman, M. J., et al. 2011, ApJ, 733, 127

Sing, D. K. 2010, A&A, 510, A21

Smith, A., Anderson, D., Skillen, I., Cameron, A. C., & Smalley, B. 2011, MNRAS, 416, 2096

Soufi, F., Goupil, M., & Dziembowski, W. 1998, A&A, 334, 911

Suárez, J., Andrade, L., Goupil, M., & Janot-Pacheco, E. 2010, AN, 331, 1073

Toomre, J., Zahn, J.-P., Latour, J., & Spiegel, E. 1976, ApJ, 207, 545

Van Eylen, V., Lund, M. N., Aguirre, V. S., et al. 2014, ApJ, 782, 14

von Essen, C., Czesla, S., Wolter, U., et al. 2014, A&A, 561, A48

Von Zeipel, H. 1924, MNRAS, 84, 665

Winn, J. N., Fabrycky, D., Albrecht, S., & Johnson, J. A. 2010, ApJL, 718, L145

Winn, J. N., Howard, A. W., Johnson, J. A., et al. 2011, AJ, 141, 63

Zwintz, K., Ryabchikova, T., Lenz, P., et al. 2014, A&A, 567, A4